6. AGE HARDENING MODEL FOR Al-7Si-Mg ALLOYS

6.1. Age hardening models

Since the precipitation of strengthening phases is critical to the properties of age-hardenable alloys, modelling of precipitation and strengthening has gained considerable interest among researchers. Various age hardening models have been developed, especially for wrought aluminium alloys [15,128-130]. In contrast to the wrought aluminium alloys, little modelling work on the age-hardening of casting aluminium alloys has been performed [82,131]. In the work of Rometsch and Schaffer [82], the methodology used by Shercliff and Ashby [15] was applied to model aging curves of Al-7Si-Mg alloys. In the work by Wu and Ferguson [131], the methodology used by Kampmann and Wagner was applied [132]. Wu and Ferguson [131] also summarised the modelling approaches of both Shercliff-Ashby and Kampmann-Wagner. The Shercliff-Ashby process model draws together established knowledge of the kinetics of microstructure evolution with dislocation behaviour in order to determine the mechanical properties. In the Kampmann-Wagner model, a numerical approach capable of describing the particle size distribution in the time domain, while dealing with the nucleation-growth-coarsening phenomena within the same formulation, is used. A strength model is then used to evaluate the resulting change in hardness or yield strength.

For the purposes of this study, the Shercliff-Ashby process model approach was used, firstly due to its relative simplicity compared to the Kampmann-Wagner approach and secondly, to allow comparison with the work of Rometsh and Schaffer on alloys A356 and A357 [82], as well as comparison with the original work of Shercliff and Ashby on alloy 6082 [15].

6.2. The Shercliff-Ashby model

Shercliff and Ashby [15] developed a process model to describe the changes in hardness or yield strength due to age hardening of heat treatable alloys. The model was successfully applied to the isothermal aging curves of wrought Al-alloys 6061 and 6082.

Included in the model are expressions for:

- the decrease in solute concentration and growth in volume fraction of precipitates during the early stages of precipitation;
- the effect of aging temperature on the equilibrium volume fraction of precipitates;
- the coarsening of precipitates by LSW ripening;
- the strength contribution from solute atoms; and
- the strength contribution from both shearable and non-shearable precipitates.

Equations describing these events are kept as straightforward as possible by combining unknown constants into physically or empirically meaningful parameters and by using dimensionless variables where possible. Only the most necessary variables to describe the microstructure and strengthening are incorporated. The methodology is consistent across the sub-models and is calibrated using experimental aging curves (i.e. making it a “mechanistic” model). Aging curves for hardness and yield strength may be calibrated equally well as some of the constants have the dimensions of yield strength and may take values in any appropriate units. As described in section 4.12, it is fundamentally more correct to make a comparison between hardness and UTS, rather than YS. However, in Fig. 4.63 it was shown that the correlation between VHN and YS in the ranges found in these alloys is acceptable.

The total Vickers hardness (VHN_t) of an Al-7Si-Mg alloy is given by equation 6.1 [15]:

$$\mathbf{VHN_t = VHN_o + \Delta VHN_{Si} + \Delta VHN_{Fe} + \Delta VHN_{ss,Si} + \Delta VHN_{ss,Mg} + \Delta VHN_{ppt,Si} + \Delta VHN_{ppt,Mg-Si}} \qquad \mathbf{(6.1)}$$

where VHN_o is the hardness of pure aluminium, ΔVHN_{Si} is the contribution to the hardness due to eutectic Si particles, ΔVHN_{Fe} from the eutectic Fe-phase particles, $\Delta VHN_{ss,Si}$ from the Si in solid solution, $\Delta VHN_{ss,Mg}$ from the Mg in solid solution, $\Delta VHN_{ppt,Si}$ from the Si precipitates and $\Delta VHN_{ppt,Mg-Si}$ due to Mg–Si precipitates.

Equation 6.1 may be simplified because ΔVHN_{Si}, ΔVHN_{Fe} and $\Delta VHN_{ss,Si}$ are expected to remain reasonably unchanged during aging. Although $\Delta VHN_{ss,Si}$ may fluctuate with aging time and temperature, these effects are expected to be negligible since changes in the Si concentration from 0.5 to 1.2 wt.% in solid solution in a binary Al–Si alloy are known to increase YS in the annealed condition by not more than 2–3 MPa [9,82]. For simplicity, it is also assumed that $\Delta VHN_{ppt,Si}$ is negligibly small, particularly in relation to the large strengthening contribution due to Mg–Si type precipitates. Accordingly, Eq. (6.1) may be simplified to:

$$\mathbf{VHN_t = VHN_i + \Delta VHN_{ss,Mg} + \Delta VHN_{ppt,Mg-Si}} \qquad \mathbf{(6.2)}$$

where VHN_i is the intrinsic strength of the alloy, which may be defined as being the sum of VHN_o and those strengthening contributions which remain invariable during aging. Potential differences in age hardening characteristics between primary α-Al and the eutectic regions are assumed as being insignificant since the α-Al phase is mostly homogenised during the solution treatment. This assumption is supported by the aging curves in Fig. 4.72 which showed that both the hardness of the eutectic and primary α-Al components increased during artificial aging.

When precipitates are small and coherent they are sheared by moving dislocations (Fig. 2.25(a)). Their contribution to the strength of the alloy involves a convolution of the resistance to shear of one particle, their population and the flexibility of the dislocations with which they interact – known as the Friedel effect [15]. It is normally accepted that the contribution to VHN by shearable precipitates (ΔVHN_s) is approximately related to the precipitate volume fraction (f) and the precipitate radius (r) through a constant c_1:

$$\mathbf{\Delta VHN_s = c_1 f^{1/2} r^{1/2}} \qquad \mathbf{(6.3)}$$

The spacing of precipitates increases during coarsening and there becomes a spacing at which the stress required to bend a dislocation (so that it bows between neighbouring particles in its slip plane, known as the Orowan mechanism) becomes less than that required to shear through them (Fig. 2.25(b)). The contribution to VHN due to the bypassing of dislocations around non-shearable precipitates (ΔVHN_b) is approximately related to the precipitate volume fraction and the precipitate radius through a constant c_2:

$$\Delta VHN_b = c_2 f^{½}/r \qquad (6.4)$$

Shercliff and Ashby [15] have shown that single-peak aging curves are satisfactorily described by taking the harmonic mean of eqs. (6.3) and (6.4):

$$\Delta VHN_{ppt,Mg-Si} = [2S(P^*)^{1/6}]/[1+(P^*)^{1/2}] \qquad (6.5)$$

where S is the precipitate strength and $P^* = P/P_p$. The term P is the “normalised temperature-corrected time”, in s/K.

$$P = t/T \exp(-Q_A/RT) \qquad (6.6)$$

where t is the aging time, T the aging temperature, Q_A the activation energy for volume diffusion of atoms through the matrix and R the gas constant (8.314 J/mol K). The parameter P_p is the value of P at the peak in the aging curve and is a constant for a given set of aging conditions.

The assumption of a single-peak aging curve is an important consideration, because it implies that only the contribution of β″-precipitation is considered. It has been shown in section 4.14 that β″-needles are mostly responsible for peak aging, with solute clusters and GP zones mainly occurring in the under-aged condition. Even though β_{rods}' was not investigated in this study, it is known that these precipitates are found in Al-7Si-Mg alloys in the over-aged condition (Fig. 2.30). By therefore only considering β″-precipitation, the expectation is that peak aging will be predicted more accurately than under- and over-aging.

The precipitate strength, S, as a function of aging time (t) and temperature (T) is expressed as follows [82]:

$$S^2(t,T) = (S_o)^2_{max}\left[1 - \exp\frac{-Q_s}{R}\left(\frac{1}{T} - \frac{1}{T_s}\right)\right]\left[1 - \exp\left(\frac{-t}{\tau_1}\right)\right] \qquad (6.7)$$

where the strength parameter $(S_o)_{max}$, the solvus enthalpy (Q_s) and the metastable solvus temperature (T_s) are determined from experimental aging data. The constant τ_1 is related to the aging time corresponding to the peak t_p by the constant K_1:

$$\boldsymbol{\tau_1 = K_1\ t} \qquad \textbf{(6.8)}$$

The solid solution hardening component $\boldsymbol{\Delta VHN_{ss,Mg}}$ in Eq. (6.2) has been described to vary with aging time as follows:

$$\boldsymbol{\Delta VHN_{ss,Mg} = [(\Delta VHN_{ss0})^{3/2} + [(\Delta VHN_{ssi})^{3/2} - (\Delta VHN_{ss0})^{3/2}]\exp(-t/\tau_1]^{2/3}} \quad \textbf{(6.9)}$$

where the subscripts refer to initial ΔVHN_{ssi} and final ΔVHN_{ss0} solid solution strengthening contributions. The initial solid solution strengthening contribution is the difference between the as-quenched hardness (VHN_q) and the intrinsic hardness (VHN_i), whereas the final solid solution strengthening contribution is the difference between the over-aged hardness (VHN_{oa}) at that aging temperature and VHN_i. VHN_{oa} may be determined from known values of VHN_q and VHN_i:

$$\boldsymbol{VHN_{oa} = VHN_i + (VHN_q - VHN_i)\exp(-2Q_s/3R)(1/T - 1/T_s)} \quad \textbf{(6.10)}$$

The contribution to the strength (or hardness) of all 3 sub-models in equation 6.2 is shown schematically in Fig. 6.1 [15]. Note that the effective mechanism of precipitation hardening is the one requiring the least shear stress, with a smooth transition between the two.

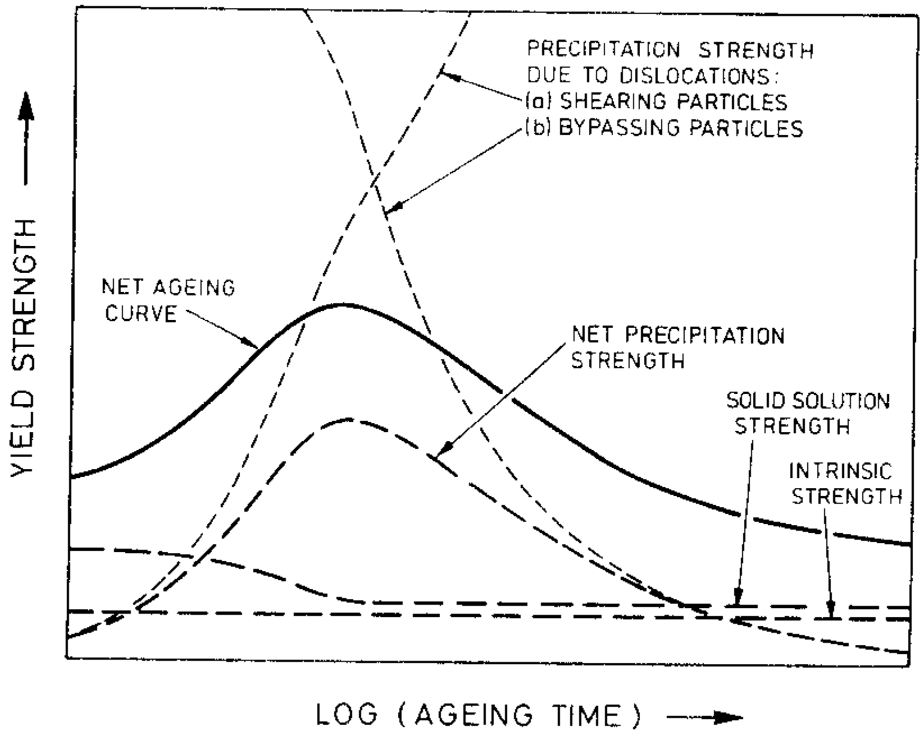

Figure 6.1: A schematic diagram of the relative contributions to the full aging curve of the intrinsic strength, solid solution strength and the precipitation hardening due to shearable and non-shearable precipitates [15].

Finally, the employment of the as-quenched hardness VHN_q implies that this model is only applicable to aging curves where no natural pre-aging has taken place, for example, it is valid for Figs. 4.28 and 4.31, but not for Figs. 4.29, 4.30, 4.32 and 4.33 of this study.

6.2.1. Calibration of the model

The steps in the calibration procedure have been summarised by Shercliff and Ashby [15]:

1) Choose values for the as-quenched hardness (VHN_q) and the intrinsic hardness (VHN_i) to calculate the first estimate of VHN_{oa} midway between the two.
2) Examine the aging curves and determine the time to reach the peak (t_p) and the peak hardness for as many different temperatures as possible.
3) Plot $\ln(t_p/T)$ vs $1/T$ and measure the gradient (Q_A/R) to find the activation energy Q_A.

4) Calculate P_p using the average of the values of the peak temperature-corrected-time.
5) For each temperature, evaluate the peak precipitation hardening increment $(\Delta VHN_{ppt,Mg-Si,})_{peak}$ and hence experimental values for S_o.
6) Plot S_0^2 vs temperature as in Fig. 6.2 and estimate T_s.
7) Estimate $(S_0)_{max}$ from the low temperature plateau in Fig. 6.2 and solve for Q_s using all the data.
8) For each temperature calculate VHN_{oa} more accurately using Eq. 6.10, then $(\Delta VHN_{ppt,Mg-Si,})_{peak}$ $(=S_0^2)$; adjust T_s, $(S_0)_{max}$ and Q_s and replot S_0^2 vs T. Repeat until the fit between theory and data is satisfactory.
9) Adjust the constant K_1 such that the solid solution part decays with an appropriate time constant τ_1 (scaled by P_p and T).

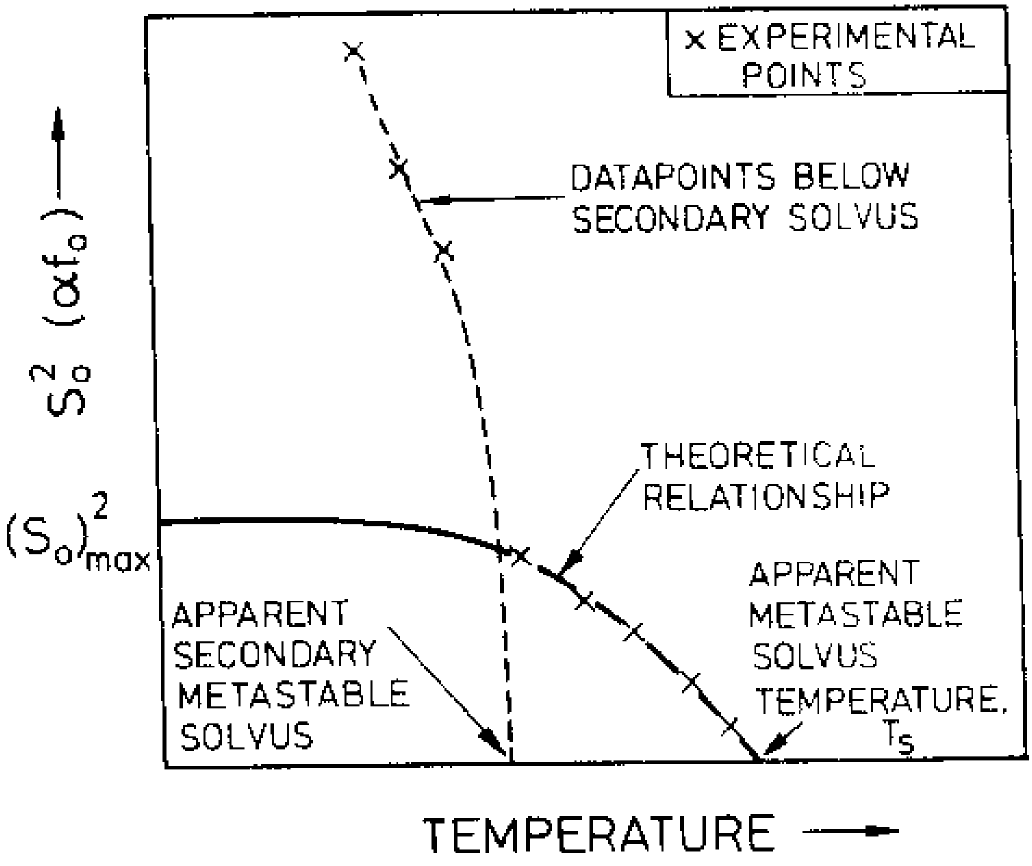

Figure 6.2: The variation of S_0^2 (which is proportional to the equilibrium volume fraction) with temperature. Typical experimental data points are shown, some of which lie at T below a secondary solvus. The solid line is the theoretical curve used to model the relationship [15].

6.2.2. Application of the model in the literature

Shercliff and Ashby [15] have applied the model to predict artificial aging hardness curves for Al-Mg-Si wrought alloy 6082 (Fig. 6.3). The agreement between theory and experimental values are good throughout, with the model fitting experimental data to within 10%.

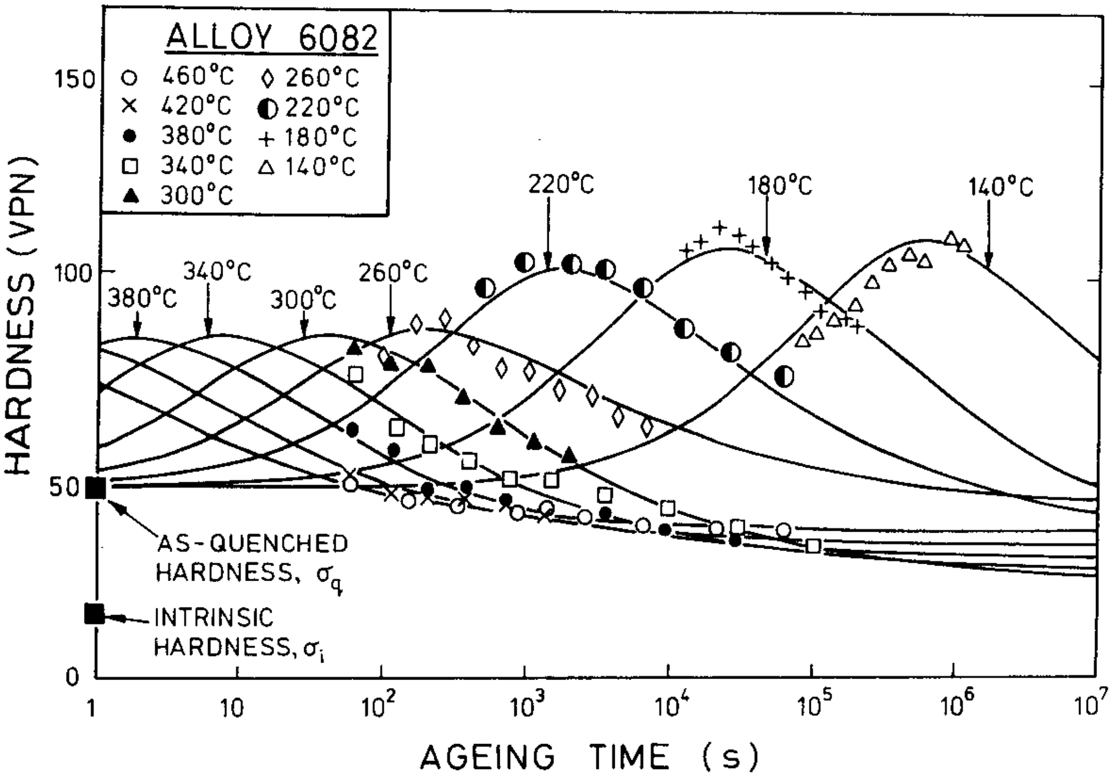

Figure 6.3: Experimental data for alloy 6082 compared with the model for nine aging temperatures [15].

Rometsch and Schaffer [82] applied the model to predict YS-aging curves for dendritic Al-7Si-Mg alloys A356 (Fig. 6.4(a)) and A357 (Fig. 6.4(b)). The modelled YS_t aging curves have more sharply defined peaks than the experimental aging curves do. The authors postulated that the broadness of the peaks in the experimental A356 and A357 aging curves suggests that under-aged and over-aged precipitates may cause more hardening than is normally assumed [82]. It is likely that, by also considering the contributions by GP zones and β′, better correlation between experimental and predicted values will be obtained.

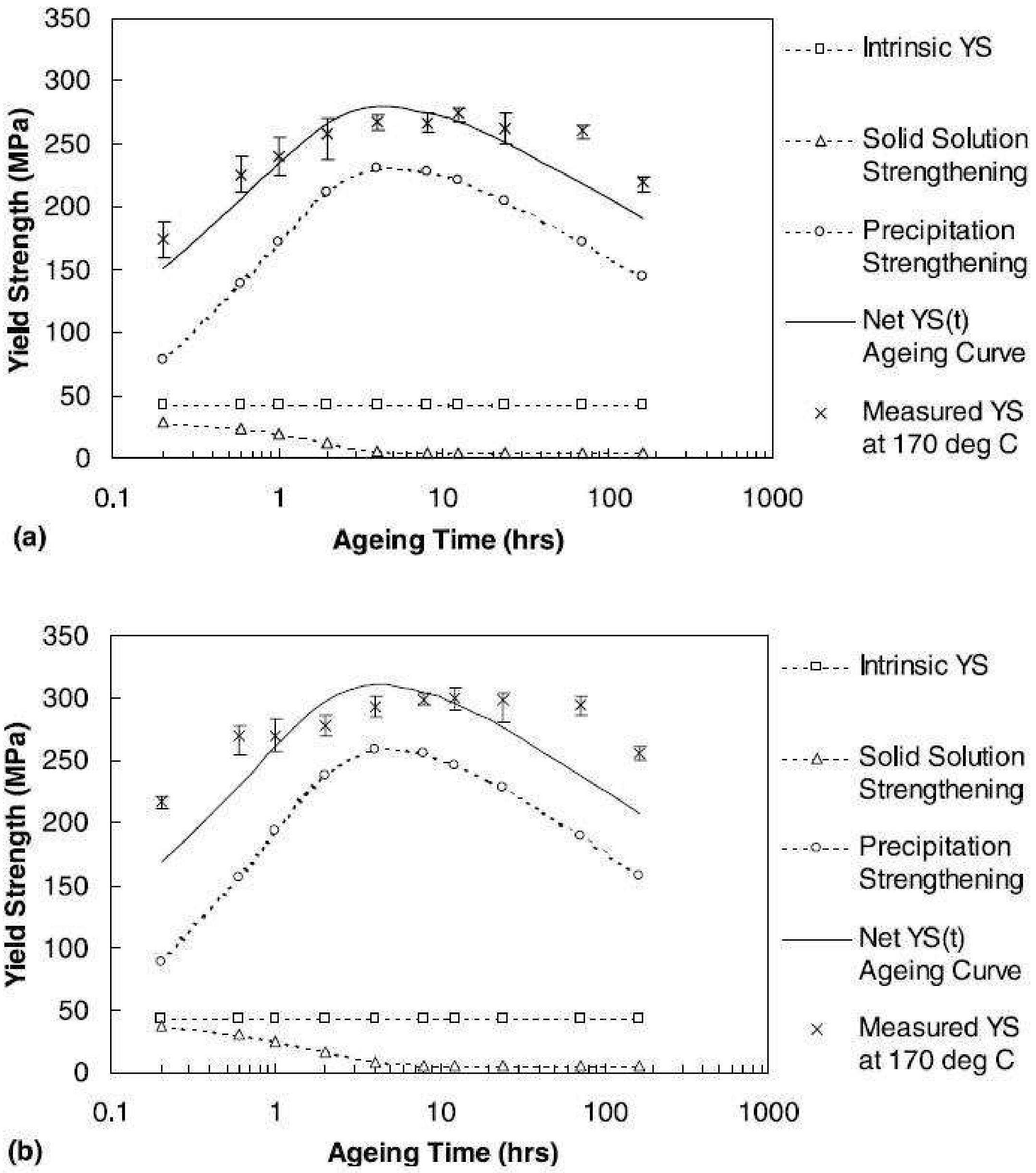

Figure 6.4: Strengthening contributions that produce the net YS_t aging curves for (a) A356 and (b) A357 at 170°C. Error bars are shown for measured YS values at 170°C [82].

6.3. Application of the model in this study

The CSIR recently successfully processed SSM-HPDC of high purity Al, even though it does not possess a solidification temperature range – Fig. 6.5 [HM13].

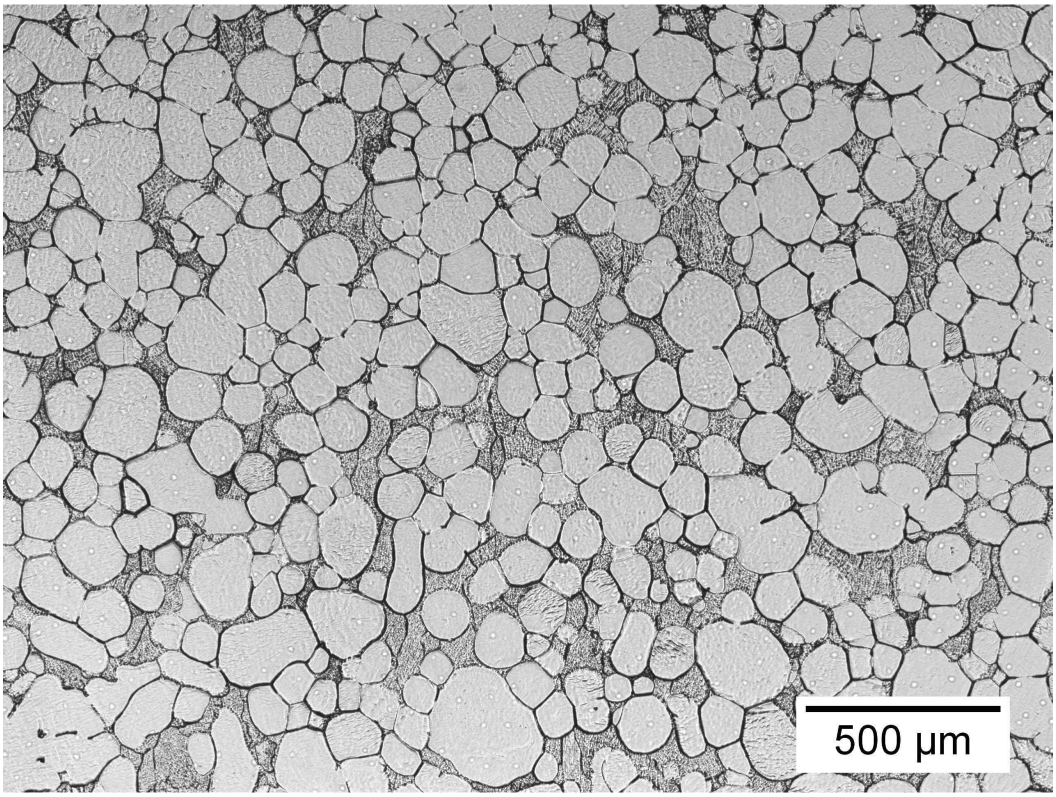

Figure 6.5: Optical micrograph of SSM-HPDC high purity Al [HM13].

The hardness of the pure Al (with globular microstructure) was measured as 19.5 VHN and this value was used as VHN_o. It corresponds reasonably well with the hardness of pure Al of 15 VHN used by Shercliff-Ashby [15]. However, the value needed for eq. 6.2 is VHN_i and not VHN_o. VHN_i is defined as being the sum of VHN_o and those strengthening contributions which remain invariable during aging. Rometsch and Schaffer [82] estimated their YS_i value from the results of Erginer and Gurland [133] who determined the YS of solution treated (100 h at 538°C) and air cooled binary Al–Si alloys containing different amounts of Si. For alloys containing 5.3% Si, the average YS was 40 MPa, whereas for alloys containing 8.5% Si, the average YS was 46 MPa; the YS_i was therefore estimated to be 43 MPa for Al–7Si alloys. To convert this YS_i to VHN_i, eq. 4.9 is used with $n = 0.188$ (Table 4.20) to give $VHN_i = 25$, which by definition must be $> VHN_o = 19.5$.

From Fig. 6.6, it can be seen that the as-quenched hardness VHN_q = ~ 53.

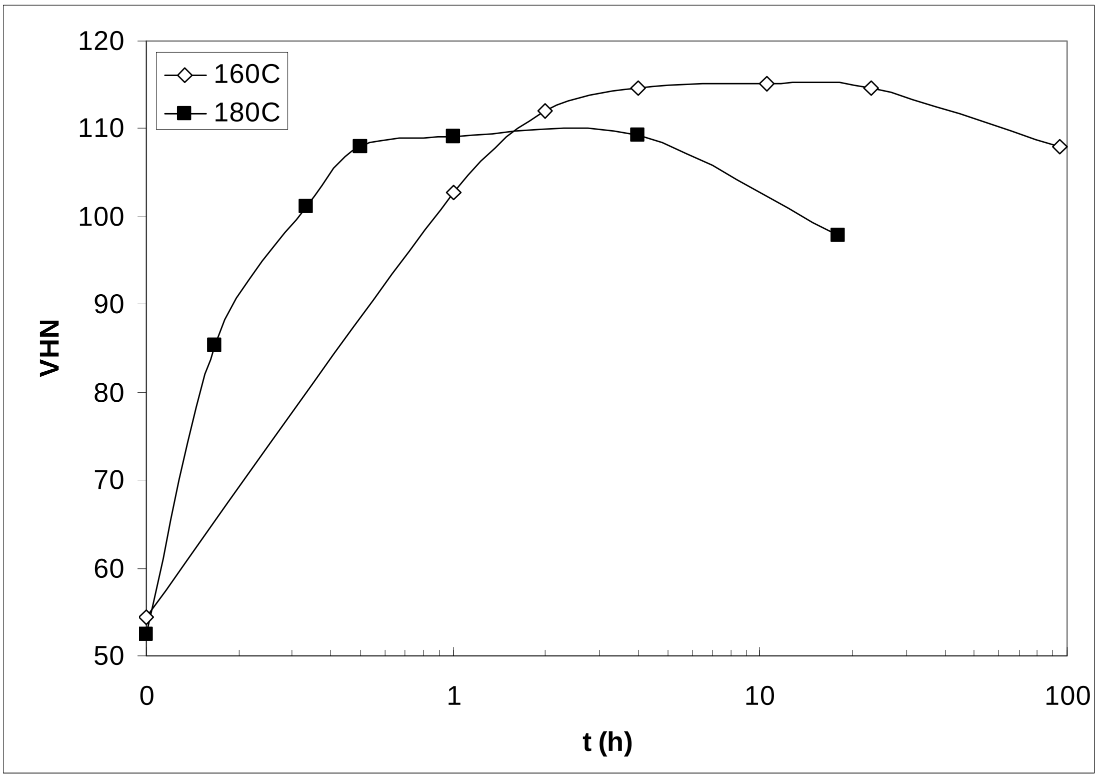

Figure 6.6: Artificial aging curves at 160 and 180°C for SSM-HPDC alloy A356 (with 0.36%Mg) showing VHN_q = ~ 53.

The first estimate of the over-aged hardness is then made midway between VHN_i and VHN_q i.e. VHN_{oa} = 39.

The activation energy (Q_A), has been determined in Fig. 4.19 as Q_A = 163 kJ/mol.
The average value of P_p is determined by using the values summarised in Table 6.1 and the initial value for S_o is determined by subtracting the estimated over-aged hardness from the peak hardness. Note that "peak time" was calculated by means of eq. 4.2 and not eq. 4.3. Eq. 4.3 gives time to maximum hardness, but not maximum YS (Table 4.23), whereas eq. 4.2 gives time to "peak" properties in terms of hardness, YS and UTS.

Table 6.1: Data for peak time and hardness, and evaluated parameters at various artificial aging temperatures.

Temperature (°C)	Time to peak (s) – eq. 4.2	P_p (s/K)	Peak VHN	S_o (VHN)
160	106200	5.32×10^{-18}	115	76
180	14400	5.09×10^{-18}	109	70
190	5400	4.75×10^{-18}	104	65
Average		**5.05×10^{-18}**		
Standard deviation		2.83×10^{-19}		

The first plot of S_o^2 vs temperature is shown in Fig. 6.7 and this gives an estimate of the metastable solvus temperature T_s = 278°C.

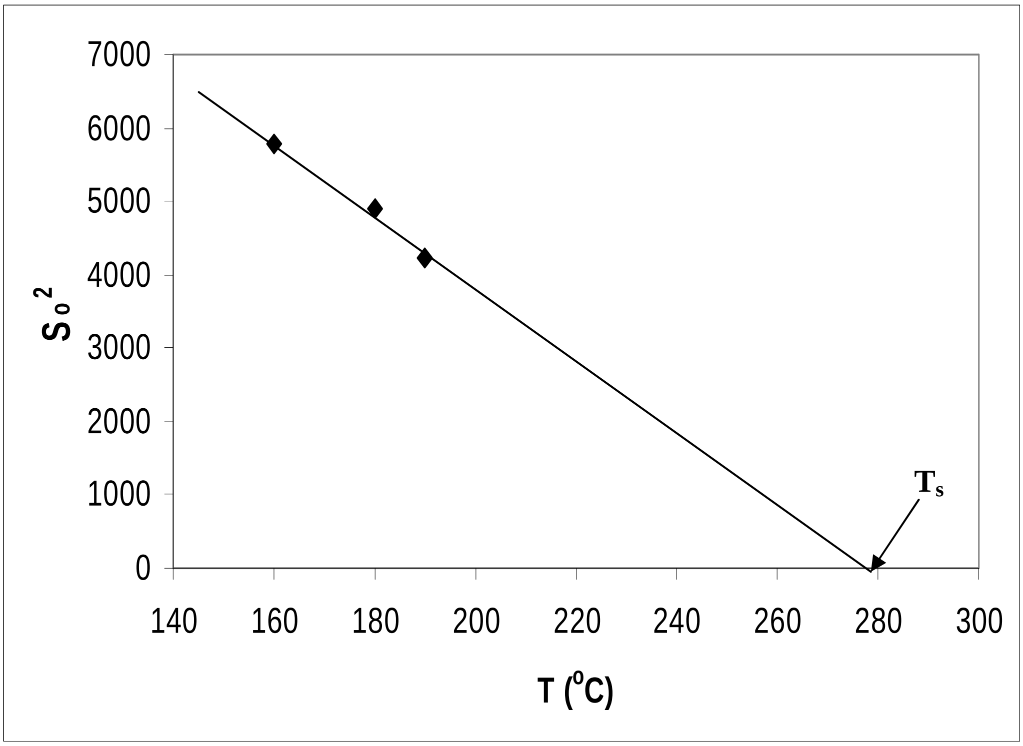

Figure 6.7: First graph of S_o^2 with temperature used to estimate T_s.

The limited number of data points in Figure 6.7 makes the determination of an accurate value for $(S_0)_{max}$ virtually impossible. The value determined by Rometsch and Schaffer [82] of 228 MPa is therefore used, which converts to VHN = 93 using eq. 4.9 with n = 0.072 (Table 4.20).

Solving equation 6.7 gives an average estimated Q_s = 18 kJ/mol. This allows a more accurate determination of VHN_{oa} = 36.2 using eq. 6.10 and a second plot of S_o^2 vs temperature can be drawn as shown in Fig. 6.8, giving an unchanged metastable solvus temperature of $T_s = 278^oC$ implying that further iterations to get a best fit of S_o^2 vs temperature are not necessary.

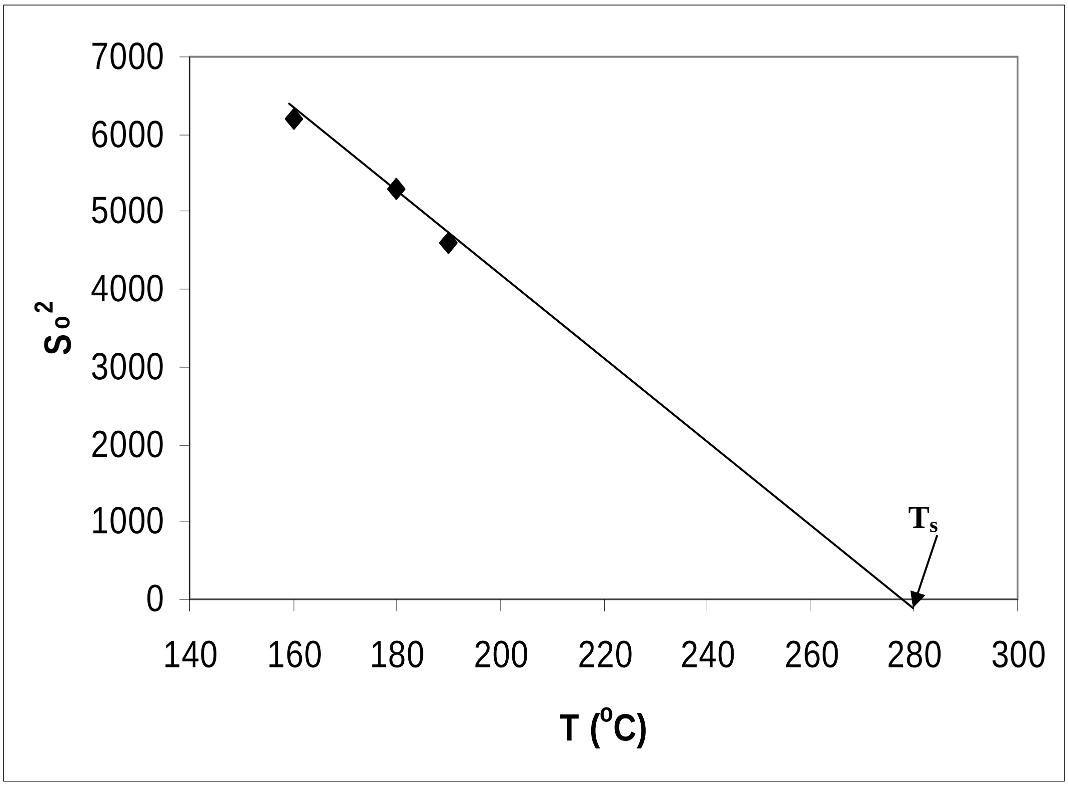

Figure 6.8: Second graph of S_o^2 with temperature used to estimate T_s.

The required decay of the solid solution component is achieved using a value of K_1 = 0.08.

A summary of the constants and calibration parameters used to model the aging curves are presented in Table 6.2. Application of the model to predict the artificial aging curves in Fig. 6.6 are shown in Fig. 6.9 for 180°C and in Fig. 6.10 for 160°C. The agreement between predicted and measured values are good, with the greatest deviation occurring at over-aged conditions, in agreement with what was also reported by Rometsch and Schaffer [82]. It needs to be recognised, however, that any model that uses experimental hardness data to set up the model and then uses that same model to compare with the same hardness data, is bound to give a good fit.

Table 6.2 Values of constants and calibration parameters used to model the aging curves.

Parameter	This study: A356
Intrinsic hardness (VHN_i)	25
As-quenched hardness (VHN_q)	53
Activation energy for aging in kJ/mol (Q_A)	163
Metastable solvus temperature in ^oC (T_s)	278
Solvus boundary enthalpy in kJ/mol (Q_s)	18
Strength parameter in VHN ($(S_o)_{max}$))	93
P_p in s/K	5.05 x 10^{-18}
K_1	0.08

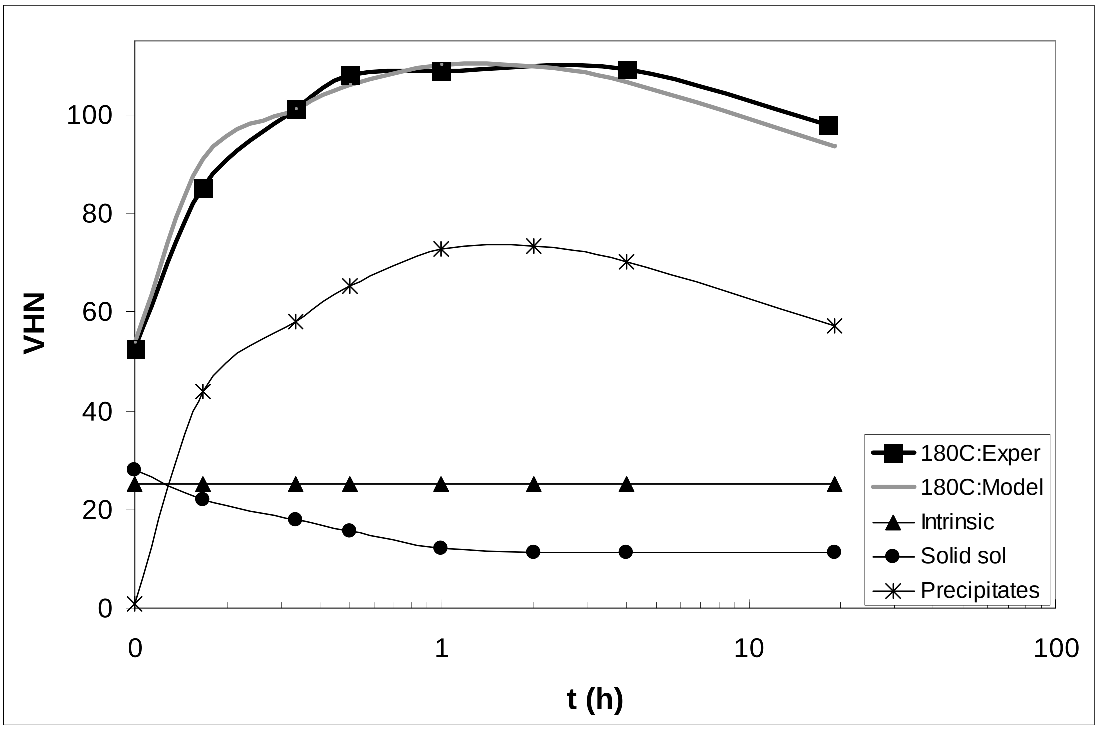

Figure 6.9: Strengthening contributions that produce the net aging curves for SSM-HPDC alloy A356 (0.36%Mg) at 180^{o}C.

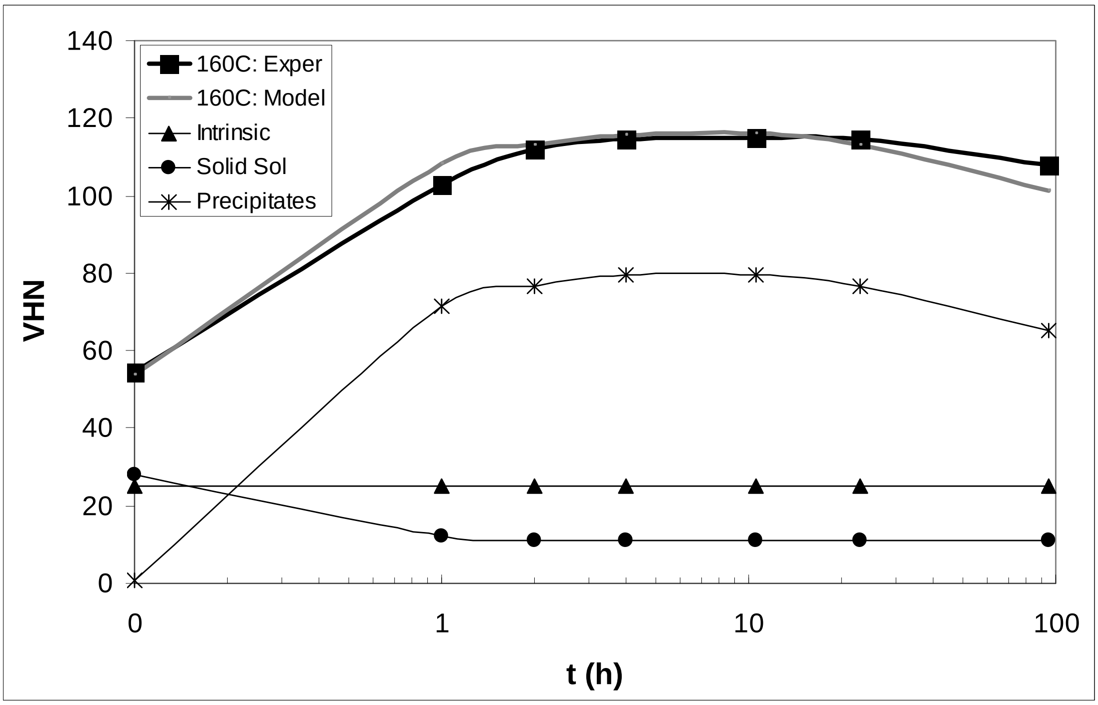

Figure 6.10: Strengthening contributions that produce the net aging curves for SSM-HPDC alloy A356 (0.36%Mg) at 160°C.

6.4. Comparison of Al-7Si-Mg casting alloy A356 to the wrought alloy 6082

Table 6.3 compares the values of constants and calibration parameters used in this study with those used by Rometsch and Schaffer [82] for alloy A356 and Shercliff and Ashby for alloy 6082 [15]. The main differences between the values found in this study and those of Rometsch and Schaffer are for Q_A and P (which are related through equation 6.6) and Q_s. As mentioned in section 4.5, the activation energy for diffusion of Mg in Al has been proposed in a range from 111 kJ/mol to 161 kJ/mol. Therefore, the experimentally determined value for Q_A of 163 kJ/mol in this study lies close to the upper limit of the range that has been proposed, with the value of 130 kJ/mol found by both [15] and [82] in Table 6.3 being within this range. The higher Q_A value in this study results in a lower P_p-value, due to their relation through equation 6.6. The Q_s value found in this study of 18 kJ/mol differs significantly from that found by Rometsch and Schaffer for A356 of 64 kJ/mol, which in turn also differs from the value found for alloy 6082 of 30 kJ/mol. These differences in Q_s might be due to the relation of Q_s with the over-aged hardness VHN_{oa} in eq. 6.10, which has been shown in Figs. 6.9 and 6.10 to be the least successfully predicted part of the aging curves.

Table 6.3 Comparison of values of constants and calibration parameters used to model the aging curves in this study with references [15] and [82].

Parameter	**This study: A356**	**Rometsch-Schaffer: A356 [82]**	**Shercliff-Ashby: 6082 [15]**
Activation energy for aging in kJ/mol (Q_A)	163	130	130
Metastable solvus temperature in ^oC (T_s)	278	271	282
Solvus boundary enthalpy in kJ/mol (Q_s)	18	64	30
Strength parameter in VHN $(S_o)_{max}$))	93	93	94
P_p in s/K	5.05×10^{-18}	3.71×10^{-14}	5.50×10^{-14}
K_1	0.08	0.11	0.50

The solvus temperatures found in Table 6.3 ranges from 271-282^{o}C, which corresponds well with the peak for β″-precipitation in the DSC curve shown in Fig. 2.33. In addition, Rometsch and Schaffer [134] have also shown by means of DSC that the β″ solvus occurs at about 270-280^{o}C. The strength parameter $(S_o)_{max}$ of 93 VHN was derived from the values found by Rometsch and Schaffer [82] and also corresponds well with the value of 94 VHN found for alloy 6082 in Table 6.3. This would suggest that similar precipitation strengthening occurs in alloys A356 and 6082. The constant $K_{1,}$ which relates τ_1 to t_p through eq. 6.8, is similar for this study and the A356 of Rometsch and Schaffer (~0.1), but significantly lower than the 0.5 for alloy 6082. The decay of the solid solution component therefore occurs faster in alloy A356 than in alloy 6082, a conclusion that is supported by the artificial aging curves presented in Fig. 4.70. As discussed in section 5.7, the excess Si in the casting alloys in this study is believed to reduce the time to initiate strengthening, presumably due to a higher driving force for nucleation which will lead to a finer particle size and shorter diffusion distances.

6.5. Modelling of artificial aging curves of SSM-HPDC Al-7Si-Mg alloys with varying Mg-contents

The parameters derived in Table 6.2 for the artificial aging curves of Figs. 6.9 and 6.10 are only applicable for a single composition – in this case the 0.36wt% Mg alloy in Table 3.1. Theoretically, to model the aging curves of the other compositions listed in Table 3.1, new parameters must be derived by determining artificial aging curves at as many temperatures as possible. This would be a very time consuming process and a simple, but accurate method to convert the aging curves of one composition to that of another composition would be beneficial.

From Fig. 4.62 it is seen that the peak hardness of Al-7Si-Mg alloys is linearly related to the (at% Mg-concentration available for precipitation hardening)$^{1/2}$. In addition, from Figs. 4.28 to 4.33 it can be seen that the shape of the aging curve is not influenced by the Mg-content of the alloy and the curve is shifted either upwards or downwards depending on the Mg-content. Therefore, using the 0.36wt% Mg alloy as a reference alloy, artificial aging curves of other alloys can be predicted using the following procedure by employing the 0.49wt% Mg alloy (Fig. 4.72) as example:

- Calculate the wt% Mg available for precipitation hardening by employing either eq. 4.4 or 4.5. For the 0.49wt% Mg alloy, eq. 4.5 must be used and the wt% Mg available for strengthening is then 0.44wt% (also ensure that the Fe-content of the alloy is ~0.1%, otherwise eq. 4.5 becomes invalid).
- Convert the wt% Mg to at% Mg. For the specific alloy in question, the at% Mg available for strengthening is calculated as 0.49at%.
- Estimate the peak hardness at 180^{o}C of this alloy by using the equation of the trend line in Fig. 4.62 (after converting the at% to at%$^{1/2}$). For the alloy in question the estimated peak hardness is 119 VHN.
- The peak hardness of the reference alloy at 180^{o}C is 109 (Fig. 6.6). Take the ratio of the peak hardness of the alloy in question to the peak hardness of the reference alloy giving 1.092.
- Keep the intrinsic hardness value VHN_i unchanged at 25, but scale the contribution of solid solution strengthening and precipitation hardening with the ratio of 1.092. The actual and predicted aging curves for the 0.49wt% Mg alloy are compared in Fig. 6.11.

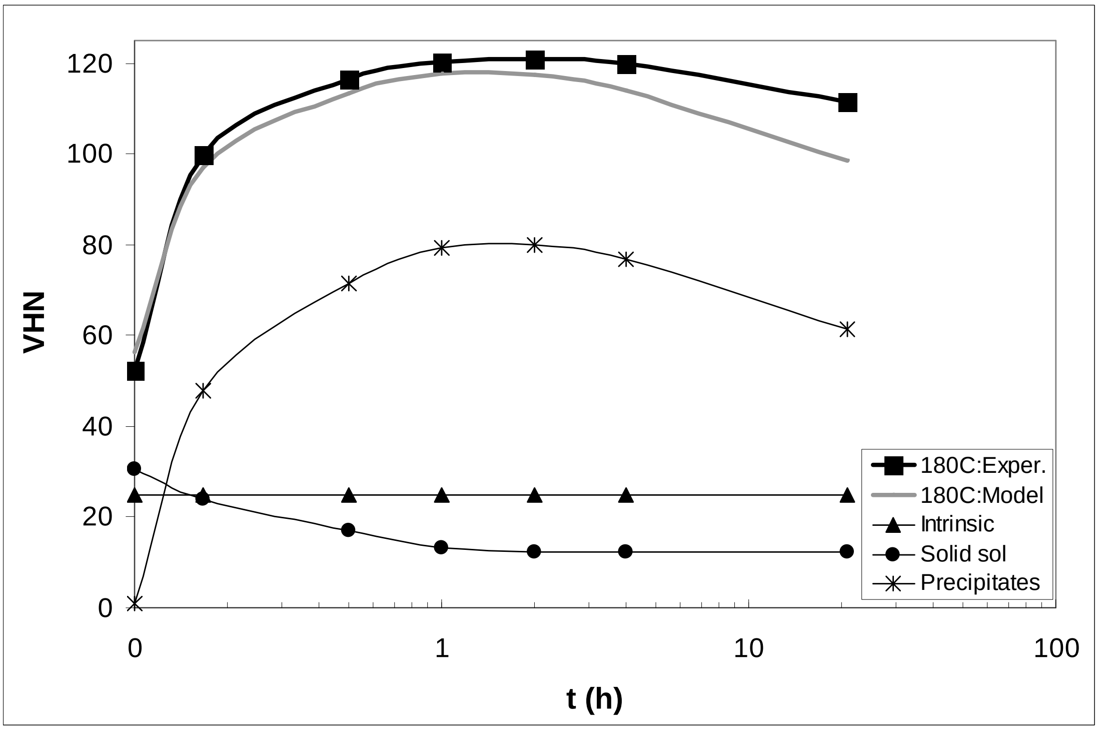

Figure 6.11: Strengthening contributions that produce the net aging curves for SSM-HPDC alloy F357 (0.49wt% Mg) at 180°C.

As before, the agreement between predicted and measured values is reasonable, with most deviation again occurring at the over-aged condition.

Artificial aging curves of alloys with less Mg than the reference alloy can also be predicted using a similar approach e.g. by employing the 0.28wt% Mg alloy (Fig. 4.28) as example:

- Calculate the wt% Mg available for precipitation hardening by employing eq. 4.4 in this case giving 0.28wt% Mg.
- Convert the wt% Mg to at% Mg which is 0.31at%.
- Estimate the peak hardness at 180°C of this alloy by using the equation of the trend line in Fig. 4.62 (after converting the at% to at%$^{1/2}$). For the alloy in question the estimated peak hardness is 101 VHN.
- The peak hardness of the reference alloy at 180°C is 109 (Fig. 6.6). Take the ratio of the peak hardness of the alloy in question to the peak hardness of the reference alloy giving 0.9266.
- Keep the intrinsic hardness value VHN_i unchanged at 25, but scale the contribution of solid solution strengthening and precipitation hardening with

the ratio of 0.9266. The actual and predicted aging curves for the 0.28wt% Mg alloy are compared in Fig. 6.12.

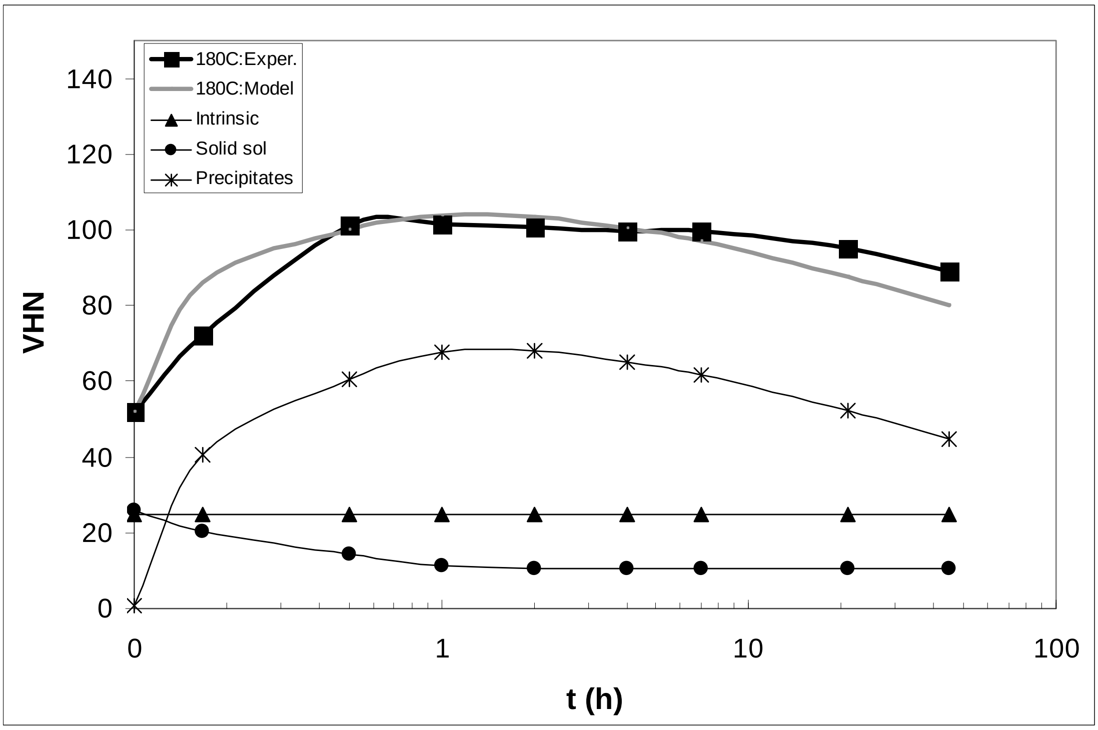

Figure 6.12: Strengthening contributions that produce the net aging curves for SSM-HPDC alloy A356 (0.28wt% Mg) at 180°C.

The agreement between predicted and measured values is good, with slight deviation again occurring in the over-aged condition, but in this case also in the under-aged condition as well. As discussed before, by only considering single peak β″-precipitation, peak aging is predicted more accurately than under- and over-aging.

7. CONCLUSIONS

7.1. SSM-HPDC

- Rheoprocessing of Al-7Si-Mg alloys with the CSIR rheocasting system results in a globular microstructure with primary α-Al globule diameters of 60-70 μm.
- High cooling rates of ~ 18°C/s are achieved during the initial stages of the HPDC step, resulting in predicted solidification being completed within 5.5s in the plate castings.
- The eutectic component in these alloys is modified by the high cooling rates achieved during HPDC, with levels of Sr as low as 14 ppm being sufficient, as opposed to about 200 ppm Sr necessary for conventional casting techniques such as permanent mould casting and investment casting.

7.2. Solution heat treatment

- The solution treatment of Al-7Si-Mg alloys has a dual beneficial effect – it causes spheroidisation of the eutectic silicon particles (improved ductility and impact properties) and it causes complete dissolution of the strengthening solutes (maximum strength after artificial aging).
- Spheroidisation of the eutectic Si particles occurs rapidly at 540°C, with their coarsening being described reasonably well by means of LSW-coarsening.
- The high cooling rates achieved during HPDC result in a high concentration of solute being retained in solid solution after casting. A solution treatment time at 540°C for only 1 h is therefore sufficient to obtain a high level of mechanical properties in the T4 and T6 temper conditions.
- The impact strength of the alloys in the T4 and T6 temper conditions is not influenced significantly by the solution treatment time (and hence the Si-interparticle spacing), but rather by the strength of the alloy.

7.3. Quench after solution treatment

- Slow quench rates after the solution heat treatment can reduce the problems of distortion and residual stresses, but also result in a loss of strength and hardness after natural- and artificial aging.

7.4. Natural aging and the T4 temper condition

- Al-7Si-Mg alloys are relatively soft directly after quenching (VHN = ~ 53), but thereafter, the hardness increases rapidly at room temperature, eventually levelling out after 4-5 days at 70-95 VHN, depending on the Mg-content of the alloy.
- Natural aging of Al-7Si-Mg alloys result in the formation of a high number density of vacancy- and Si-rich Si-Mg clusters with a significantly lower number density of GP zones and no β″-needles.
- The solute clusters are fully coherent with the matrix and they have a low Mg:Si ratio of ~ 0.6-0.7.

7.5. Artificial aging and the T5 temper condition

- The relatively fast cooling rates achieved with HPDC result in an adequate quantity of solutes remaining in solid solution after casting, which allows a reasonable response to age hardening in the T5 temper condition.
- No spheroidisation of the eutectic Si occurs in the T5 condition due to the lack of a solution treatment step, causing relatively low elongation and impact strength.

7.6. Artificial aging and the T6 temper condition

- Artificial aging at lower temperatures (e.g. 160°C) produces slightly higher peak hardnesses compared to artificial aging at higher temperatures (e.g. 180°C), but the time-to-peak hardness is significantly increased.
- The time required to obtain maximum hardness at different artificial aging temperatures can be predicted using Arrhenius-type equations.
- When no natural pre-aging occurs, a hardness plateau is maintained once the maximum hardness is reached during artificial aging at 180°C after about 1 to 5 hours. This differs from when natural pre-aging occurs when a hardness peak is observed after approximately 4 hours.
- The effects of any natural aging can largely be removed by an artificial aging treatment of 180°C for 4 hours.

7.6.1. Artificial aging without natural pre-aging

- A high concentration of solute and quenched-in vacancies leads to rapid formation of clusters and GP zones → transformation to relatively small β″-needles at the start of the hardness plateau → coarsening of β″-needles during the hardness plateau. This depletes the matrix from Mg and Si, while increasing the Mg:Si ratio of the precipitates, whilst retaining only a few clusters and GP zones. This results in constant hardness and UTS, but increasing YS.

7.6.2. Artificial aging with natural pre-aging

- Coarsening of the room temperature clusters → spherical GP zones → β″-needles, coinciding with a decrease of the matrix Mg and Si content and an increase in Mg:Si ratio of the precipitates, while retaining a relatively high number density of room temperature Si-rich clusters and GP zones that remain durable during artificial aging.

7.6.3. Characteristics of precipitates found in Al-7Si-Mg alloys

- **Solute clusters**

  The Si-rich room temperature clusters are durable at artificial aging temperatures of 180°C, even at a time of 4 h that corresponds to the peak aged condition.
- **GP zones**

  The GP zones are approximately 2 nm in diameter and are fully coherent with the matrix. The Mg:Si ratio of GP zones of 0.8-1.1 is higher than those of the solute clusters, which indicates that Mg-diffusion is rate limiting during precipitation.
- **β″-needles**

  The β″-needles range in size from ~ 2 nm diameter x 10 nm length early during artificial aging to ~ 4 nm diameter x 25 nm in the peak aged condition. The β″-needles have the highest Mg:Si ratio of all the precipitates due to the precipitation process being controlled by Mg-diffusion with the needles with > 1200 solute atoms having a Mg:Si ratio of ~ 1.0 – 1.2.

7.7. Influence of chemical composition fluctuations

- The strength and macrohardness values of Al-7Si-Mg alloys show good linear relationships to (at% Mg-concentration available for precipitation hardening)$^{1/2}$.
- Higher Mg-levels (> 0.4wt%) in Al-7Si-Mg alloys increase the stability range of the Mg-containing π–phase to higher temperatures, and suppress the Mg-free β–$FeSiAl_5$ phase at high temperatures.

- The stability of the π-phase in alloy F357 causes a reduction in the amount of magnesium in solid solution. This has a detrimental effect on the aging behaviour of this alloy compared to alloy A356.
- High Fe-levels above specification (> 0.20%) in alloy F357 result in the formation of high volume fractions of intermetallics such as π-$Al_8FeMg_3Si_6$ and β-Al_5FeSi. Micro-cracking of these intermetallics during tensile testing causes a marked reduction in ductility.

7.8. Comparison of the aging response of globular and dendritic Al-7Si-Mg alloys

- The natural aging (T4) and artificial aging (T6) responses of Al-7Si-Mg alloys are not influenced by having a globular or dendritic microstructure.
- Provided that the maximum quantity of the alloy’s Mg is placed into solid solution during solution treatment, and that the alloy’s Fe content is within specification, the response to age hardening of Al-7Si-Mg alloys should be independent of the processing technique used.
- The frequently specified artificial aging parameters of 160°C for 3-6 h or 170°C for 6 h for both dendritic and globular Al-7Si-Mg alloys will result in large variations in properties depending on the natural pre-aging period. Parameters of 180°C for 4 h are proposed as an alternative to overcome this shortcoming.

7.9. Comparison of the aging response of Al-7Si-Mg alloys with 6000 series wrought alloys

- Conventional casting alloys A356 and F357 obtain the same level of strength (hardness) in the T6 temper regardless of the prior natural aging period employed over a relatively wide range of Mg compositions. Alloy 6082 (with relatively high Si and Mg contents for a 6000 series alloy) displays a much reduced strength and hardness in the T6 condition following natural aging. Alloy 6004 (with relatively low Mg and Si) displays the opposite behaviour.
- The high Si content of the conventional casting alloys compared to the 6000 wrought series alloys results in a faster artificial aging response (shorter T6 aging cycles), higher strength for comparable Mg contents and less sensitivity to prior natural aging on peak strength. However, over-aging occurs earlier in the casting alloys than for the wrought alloys.

7.10. Age hardening model for Al-7Si-Mg alloys

- The Shercliff-Ashby methodology was followed to successfully predict artificial aging curves (with no natural pre-aging) of Al-7Si-Mg alloys.
- A method to allow prediction of artificial aging curves with Mg-contents different from that of the reference alloy has been proposed.

8. RECOMMENDATIONS

Based on the results of this study, the following recommendations for future research are made:

8.1. SSM-HPDC

- The surface liquid segregation (SLS) layer found in castings produced by means of SSM-HPDC has been noted during this study. The effects of this SLS layer on mechanical properties, but especially surface-sensitive properties such as fatigue and corrosion, need to be investigated.

8.2. Solution heat treatment

- Even though the impact strength of the alloys in the T4 and T6 temper conditions is not influenced significantly by the solution treatment time, the effects on other properties such as fatigue, creep and corrosion (which also includes stress corrosion cracking and corrosion fatigue), must be characterised.

8.3. Quench after solution treatment

- More data points at lower cooling rates during quenching of SSM-HPDC Al-7Si-Mg alloys after solution heat treatment would be beneficial, as well as quantification of distortion and the development of residual stresses.

8.4. Artificial aging and the T5 temper condition

- The relatively fast cooling rates achieved with HPDC has not been utilised to the full for the T5 temper condition in this study due to too long intensification times being employed during HPDC. Optimisation of intensification parameters and subsequent quenching should result in a more improved response to age hardening in the T5 temper condition.
- APT was done only on samples in the T4 and T6 temper conditions in this study. APT analyses of samples in the T5 temper condition (i.e. air cooled or water quenched after HPDC, with or without natural pre-aging and artificially aged at different temperatures and times) would reveal the influence of different levels of supersaturation on the nanostructural evolution during aging.

8.5. Artificial aging and the T6 temper condition

- APT was done only on samples artificially aged at 180°C for times up to 4 h in this study. APT analyses revealing the transformation of $\beta_{needles}''$ to β_{rods}' to β_{plates} in over-aged samples ($t > 4$ h at 180°C) would be beneficial.
- APT analyses of samples artificially aged at lower and higher temperatures than 180°C would quantify how the differences in solubility and hence supersaturation would lead to different nucleation rates and volume fractions of strengthening phases.

8.6. Influence of chemical composition fluctuations

- The strength and macrohardness values of Al-7Si-Mg alloys show good linear relationships to (at% Mg-concentration available for precipitation hardening)$^{1/2}$. The APT analysis in this study was only performed for a single Al-7Si-Mg alloy. APT analyses on alloys with varying Mg-contents (but constant Fe-contents) should quantitatively reveal the origin of this linear relation.

8.7. Age hardening model for Al-7Si-Mg alloys

- The Shercliff-Ashby methodology can be improved by not only considering the $\beta_{needles}''$ (peak aging), but also considering the effects of solute clusters and GP zones (under-aging) and β_{rods}' and β_{plates} (over-aging).